Article

Synthesis, Structural, and Mechanical Behavior of β-Ca$_3$(PO$_4$)$_2$–ZrO$_2$ Composites Induced by Elevated Thermal Treatments

Nandha Kumar Ponnusamy [1,2], **Hoyeol Lee [2]**, **Jin Myoung Yoo [1]** and **Seung Yun Nam [1,2,*]**

1   Industry 4.0 Convergence Bionics Engineering, Pukyong National University, Busan 48513, Korea;
     nandhabiochem@gmail.com (N.K.P.); hoyeollee11@gmail.com (H.L.); jinmyoungyoo@gmail.com (J.M.Y.)
2   Department of Biomedical Engineering, Pukyong National University, Busan 48513, Korea
*   Correspondence: synam@pknu.ac.kr; Tel.: +82-51-629-5776

Abstract: Biocompatible β-Ca$_3$(PO$_4$)$_2$ and mechanically stable t-ZrO$_2$ composites are currently being combined to overcome the demerits of the individual components. A series of five composites were synthesized using an aqueous precipitation technique. Their structural and mechanical stability was examined through X-ray diffraction, Rietveld refinement, FTIR, Raman spectroscopy, high-resolution scanning electron microscopy, and nanoindentation. The characterization results confirmed the formation of β-Ca$_3$(PO$_4$)$_2$–t-ZrO$_2$ composites at 1100 °C. Heat treatment above 900 °C resulted in the degradation of the composites because of cationic interdiffusion between Ca^{2+} ions and O^{-2} vacancy in Zr^{4+} ions. Sequential thermal treatments correspond to four different fractional phases: calcium-deficient apatite, β-Ca$_3$(PO$_4$)$_2$, t-ZrO$_2$, and m-ZrO$_2$. The morphological features confirm in situ synthesis, which reveals abnormal grain growth with voids caused by the upsurge in ZrO$_2$ content. The mechanical stability data indicate significant variation in Young's modulus and hardness throughout the composite.

Keywords: β-tricalcium phosphate; zirconia; calcium-deficient apatite; composites; phase transition; sintering

1. Introduction

Bone defects caused by traumas, congenital disabilities, fatigue loading, and sarcomas are severe problems for individuals that significantly reduce their quality of life. The clinicians use autograft (bone donation from the same person) and allograft (cadaver bone) techniques to treat bone defects [1,2]. However, traditional bone grafts have several disadvantages: postoperative infection, disease transmission, insufficient donor sites, morbidity from the donor site, high costs, and limited accessibility. To overcome these disadvantages and the increased demand for bone-graft substitutes, the researchers focus on synthetic bone-graft materials that have the prerequisite of owning excellent biocompatibility and mechanical features [3,4]. Metallic implant materials have been used as artificial implants that involved the usage of stainless steel (316L SS) and titanium alloys (Ti metal and Ti-6Al-4V) for the last decades. However, these metallic implants are prone to high corrosion rates in a hostile human physiological environment, which has led to the development of alternative materials in the form of ceramics [5].

Phosphate-based ceramics are studied for bone-graft substitutes because of their biocompatibility in a hostile environment and their ability to facilitate bone regeneration in host tissues [6,7]. Hydroxyapatite (HA, Ca$_{10}$(PO$_4$)$_6$(OH)$_2$) and tricalcium phosphate (TCP, Ca$_3$(PO$_4$)$_2$) are gaining much attention as bone-graft substitutes. These materials are chemically similar to bone tissue, biocompatible, and osteoconductive [8–10]. However, phosphate-based ceramics have disadvantages, such as phase degradation during thermal treatments and poor mechanical stability [11,12]. Consequently, many researchers have

investigated several methods of reinforcing calcium phosphate using bioinert materials, including zirconia. Incorporating bioinert materials in calcium phosphate increases the mechanical properties, such as hardness, toughness, and the fracture toughness in the composites [13]. Zirconia is one of the most desirable implants because of its high bio-compatibility, chemical resistance, hardness, and fracture toughness [14,15]. Pure zirconia exhibits three forms of allotropy during thermal treatment, namely the monoclinic (m-ZrO_2, $25-1170$ °C), tetragonal (t-ZrO_2, 1170–2370 °C), and cubic (c-ZrO_2, 2370 °C–melting point) phases. During cooling, the zirconia form can be reverted to its initial phase. Among these polymorphs, tetragonal zirconia (t-ZrO_2) is suitable for hard tissue replacement because of its mechanical stability, that is, its high hardness (H ~ 18 GPa) and Young's Modulus (E ~ 255 GPa) [16,17].

Several approaches for reinforcement using a biocompatible calcium phosphate matrix and zirconia material have been investigated to improve bone regeneration and mechanical stability. From the recent report, Cao et al. [18] prepared a mixture of HA and 3YSZ sourcing by a flash sintering process to elude the phase degradation and promote the densification for mechanical stability. The presence of 60% 3YSZ content and the gradual decomposition of HA lead to pores, lack in densification, uneven grains, and secondary formations. From the same group, Cao et al. [13] investigated HA-ZrO_2 scaffolds; during the sintering process, a lack of phase stability and the scaffold embedded in stimulated body fluids in the resultant 10 wt% shows better compressive strength. Shaianlou et al. [19] established incorporating graphene oxide (GO), HA, and ZrO_2 in scaffold fabrication followed by a simulated body-fluid solution to strengthen the composites mixture. The compressive strength shows a reductant incomparable with GO/ZrO_2 composites. However, during thermal treatments, the preliminary HA and ZrO_2 mixture undergoes phase degradation, which leads to the formation of a secondary phase, including β-$Ca_3(PO_4)_2$, CaO, $CaZrO_3$, $Ca_4(PO_4)_2O$, and α-$Ca_3(PO_4)_2$ [20–22]. Furthermore, the secondary phase grains are impregnated on the lattice site of the composites, thus degrading the mechanical stability [23,24]. Considering the drawback of HA, bioactive tricalcium phosphate can be an alternative substitute because of its excellent biocompatibility and osteoconductive properties. The combination of inert materials such as β-$Ca_3(PO_4)_2$–TiO_2 and β-$Ca_3(PO_4)_2$–Al_2O_3 have recently been reported to improve the structural stability by elevating temperatures. Composites with stable phases have garnered attention because of their exceptional mechanical stability, antibacterial property, and low friction with living tissues [25,26]. The partially stabilized zirconia's mechanical strength can be attributed to enhancing the physicochemical property of the composites mixtures.

The current study aims to develop and fabricate the $Ca_3(PO_4)_2$ and ZrO_2 composites without using additive agents to improve mechanical and thermal stability. A wide range of various composites was prepared via in situ synthesis methods. The investigation involves detailed structural analysis, followed by investigations of the microstructural and mechanical stability of the $Ca_3(PO_4)_2$–ZrO_2 composites.

2. Materials and Methods

2.1. Powder Synthesis

Simple wet precipitation techniques were utilized for the preparation of $Ca_3(PO_4)_2$–ZrO_2 composites with different composition ratios by varying the ZrO_2 precursor concentration. All the chemicals, including $Ca(NO_3)_2$, $(NH_4)_2HPO_4$, and $ZrOCl_2$, were purchased from Sigma Aldrich (St. Louis, MO, USA), and five composite combinations were formulated for powder synthesis. Pure TCP with a Ca/P ratio of 1.5 for comparative purposes and variations in the ZrO_2 precursor concentration are represented by samples codes, as shown in Table 1. Powder synthesis was conducted by the addition of the prepared cationic precursors Ca^{2+} and Zr^{4+}. This was mixed as the $(NH_4)_2HPO_4$ anion precursor was slowly added dropwise to the cationic solution; stirring was maintained at 250 RPM and the operating temperature was fixed at 90 °C for the entire reaction. Afterward, the NH_4OH solution was added to maintain approximately pH 8, with further stirring for 2 h. The precipitate

samples were filtered via vacuum filtration and dried in a hot-air oven (TECHNICO OVEN, Technico Laboratory Products Pvt. Ltd., Chennai, India) at 120 °C for 24 h. The precipitate dried powder was crushed with a mortar and pestle to obtain a fine powder. The desiccated composite powder was prepared for heat treatment in a muffle furnace (MATRI-MC 2265 A, Matri Instruments & Chemicals Pvt. Ltd., Puducherry, India) at a heating rate of 5 °C min^{-1} and atmospheric conditions for a 2 h dwell time.

Table 1. Chemical composition of the prepared β-$Ca_3(PO_4)_2$–ZrO_2 composites.

	Precursor Concentration in a Molar Ratio (mol L^{-1})				
Sample Code	**$Ca(NO_3)_2 \cdot 4H_2O$**	**$NH_4H_2PO_4$**	**$ZrOCl_2 \cdot 8H_2O$**	**Ca/P**	**(Ca + Zr)/P**
Pure TCP	1.0 M	0.6667	-	1.50	1.500
1CPZ	1.0 M	0.6667	0.2	1.50	1.800
2CPZ	1.0 M	0.6667	0.4	1.50	2.100
3CPZ	1.0 M	0.6667	0.6	1.50	2.400
4CPZ	1.0 M	0.6667	0.8	1.50	2.700
5CPZ	1.0 M	0.6667	1.0	1.50	3.000

2.2. Physiochemical Characterization

The heat-treated $Ca_3(PO_4)_2$-ZrO_2 composites were qualitatively analyzed and characterized via X-ray diffraction analysis (Ultima IV, Rigaku, Tokyo, Japan) using Cu Kα radiation (λ = 1.5406 Å) at 40 kV and 30 mA. The diffraction angles (2θ) between 10 and 70° were scanned with a step size of 0.02° 2θ per second. Phase determinations were conducted using the standard International Centre for Diffraction Data (ICDD) Card Nos. 00-009-0169 (β-$Ca_3(PO_4)_2$), 00-009-0432 ($Ca_{10}(PO_4)_6(OH)_2$), 01-079-1765 (*t*-ZrO_2), and 01-083-0944 (*m*-ZrO_2). The vibrational modes of the composite powders were determined from the backscattering geometry of the confocal Raman microscope (Renishaw, Gloucestershire, UK). All the composite powder samples were excited at a wavelength of 785 nm by a semiconductor diode laser (0.5% of power) at a data acquiring time of 30 s. Fourier transform infrared spectroscopy (FT-IR) in the transmission mode was performed using an FT-IR spectrophotometer (PerkinElmer, Shelton, CT, USA); in the IR region (4000$-$400 cm^{-1}), it was performed via the KBr method to determine the functional groups in the heat-treated composite powders. The microstructural features of the β-$Ca_3(PO_4)_2$–ZrO_2 composites were determined through high-resolution scanning electron microscopy (HRSEM; FEG-200, FEI-Quanta, Eindhoven, Netherlands). The procedure described in our earlier reports was utilized in the mechanical study [26,27]. Nanoindentation (CETR, Campbell, CA, USA) was performed using the mechanical data to determine the Young's modulus and hardness for the 1100 °C heat-treated composites. The schematic representation of the synthesis and fabrication process of the β-$Ca_3(PO_4)_2$–ZrO_2 composites is shown in Figure 1

Quantitative studies were conducted via Rietveld refinement analysis using GSAS-EXPGUI (V1208, National Laboratory, Los Alamos, NM, USA) software for complete refinement analysis. The standard crystallography information files (CIFs) data were obtained from the American Mineralogist database [28]. The CIF for β-$Ca_3(PO_4)_2$ was obtained from Yashima et al. [29] and a detailed description covering the rhombohedral setting, space groups, and lattice parameters were used for refinement analysis; R3c, Z = 21, a = 10.4352 Å, and c = 37.4029 Å. The atomic arrangement of β-$Ca_3(PO_4)_2$ includes 18 independent atomic positions: 5 Ca positions (3 in site 18b and 2 in site 6a at one-half occupancy), 3 P positions (2 in site18b and 1 in site 6a), and 10 O positions (9 in site 18b and 1 in site 6a). The corresponding CIF data were obtained for HA, *t*-ZrO_2, and *m*-ZrO_2 [30–32].
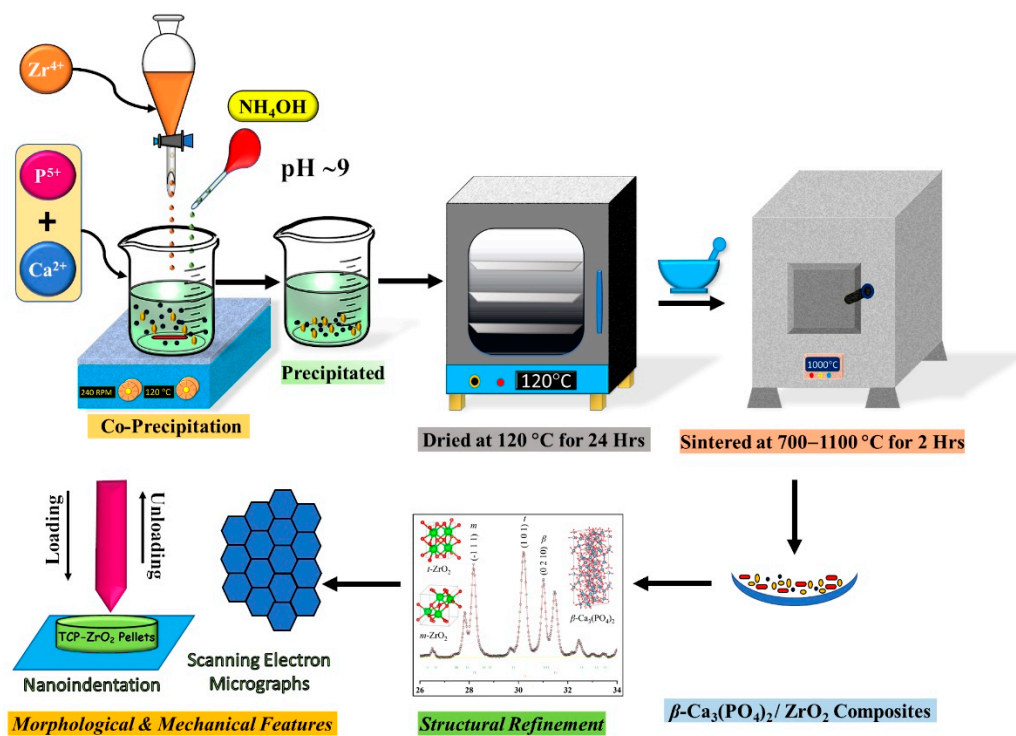
Figure 1. Schematic illustration of the synthesis and fabrication of the β-Ca$_3$(PO$_4$)$_2$–ZrO$_2$ composites.

3. Results

3.1. X-Ray Diffraction Analysis

Pure TCP powder with a Ca/P ratio of 1.5 was compared with five different β-Ca$_3$(PO$_4$)$_2$–ZrO$_2$ composites during the preliminary synthesis. The X-ray diffraction pattern of the powder composites after heat treatment at 700 °C (Figure 2a) was evaluated. A calcium-deficient apatite (CDA) phase was observed in the pure β-TCP; a surplus apatite phase and higher crystallization corresponded to an increase in the ZrO$_2$ concentration. Generally, the CDA is observed in the β-Ca$_3$(PO$_4$)$_2$ at 780 °C. The XRD pattern is in good agreement with the existing standard ICDD reference cards. Furthermore, the pattern observed in the composites at 700 °C was verified by heating to 900 °C.

The XRD reflection pattern reveals that the apatite formed during the β-Ca$_3$(PO$_4$)$_2$ phase was observed in the pure TCP and accompanied the initial formation of apatite in the β-Ca$_3$(PO$_4$)$_2$ composites. Likewise, crystallization occurs in ZrO$_2$ and is observed in the allotropy phase for t-ZrO$_2$ and m-ZrO$_2$ at 900 °C. Furthermore, a steady increase in the ZrO$_2$ content and a decrease in the apatite phase are clearly observed in the XRD reflection pattern at 900 °C (Figure 2b). The existence of the apatite phase, which is inimical to the crystallization of the β-Ca$_3$(PO$_4$)$_2$ phase, was observed in the XRD pattern at 900 °C. Moreover, XRD patterns were recorded for the samples treated at 1000 °C. The reflection patterns reveal the presence of β-Ca$_3$(PO$_4$)$_2$. Along with predominant peaks, dual-phase m-ZrO$_2$, t-ZrO$_2$, and the apatite phase are observed at 1000 °C (Figure 2c). The XRD reflection pattern at 1100 °C reveals diffracted peaks corresponding to β-Ca$_3$(PO$_4$)$_2$, m-ZrO$_2$, and t-ZrO$_2$ and an increase in zirconia concentration. The augmentation peak intensity corresponded to m-ZrO$_2$ and t-ZrO$_2$, and a decreasing trend is observed for β-Ca$_3$(PO$_4$)$_2$. The β-Ca$_3$(PO$_4$)$_2$–ZrO$_2$ composites revealed the complete removal of the apatite phase at 1100 °C (Figure 2d).

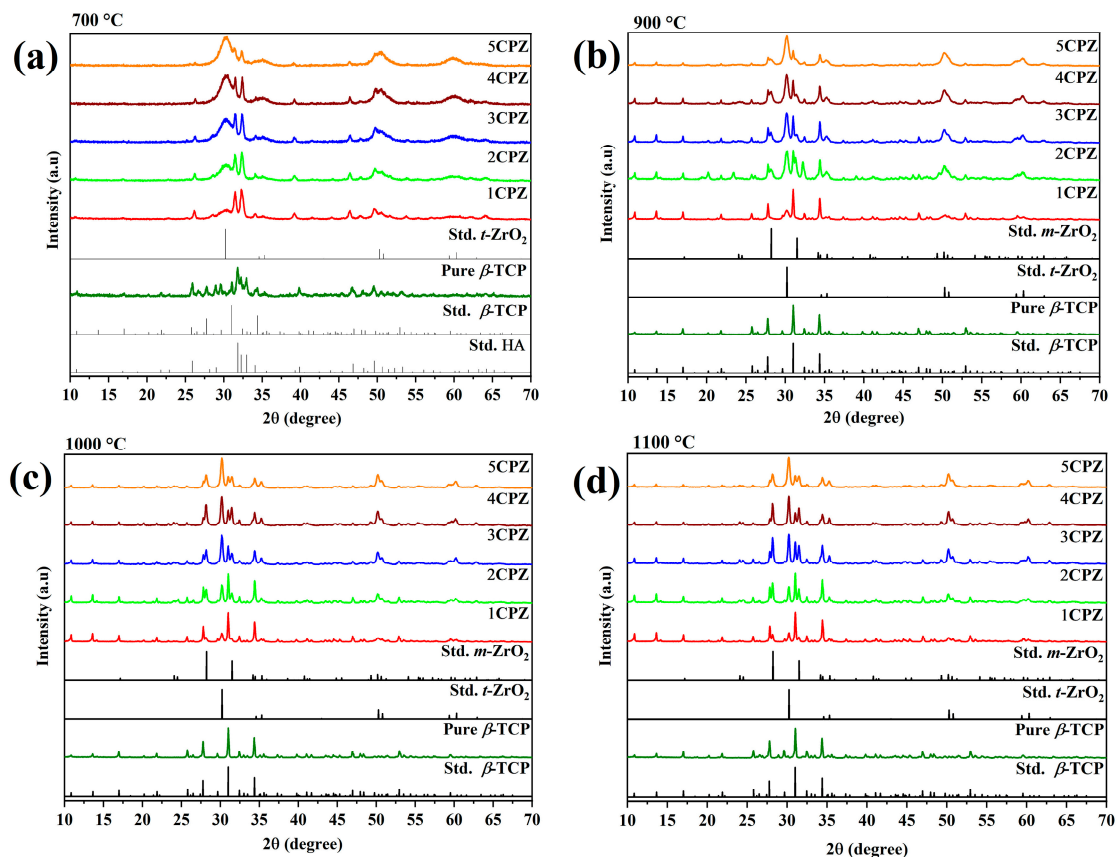**Figure 2.** The figures represent the X-ray diffraction of β-Ca$_3$(PO$_4$)$_2$–ZrO$_2$ composites heat-treated at (**a**) 700 °C, (**b**) 900 °C, (**c**) 1000 °C, and (**d**) 1100 °C, respectively. The diffraction standard for HA-Ca$_{10}$(PO$_4$)$_6$(OH)$_2$, β- Ca$_3$(PO$_4$)$_2$, *t*-ZrO2, and *m*-ZrO2 is represented by ICDD Card Nos: 00–009–0432, 00–009–0169, 01–079–1765, and 00–083–0944, respectively.

3.2. Raman Spectroscopy

The Raman spectra were measured for the β-Ca$_3$(PO$_4$)$_2$–ZrO$_2$ composite at three different temperatures. The Raman bands were observed at 700 °C (Figure 3a) for the apatite phase, with bands at ~960 cm^{-1} (ν_1 mode), 430 and 447 cm^{-1} (ν_2 modes), ~1026 and 1076 cm^{-1} (ν_3 modes), and 579, 591, and 615 cm^{-1} (ν_4 modes). Moreover, β-Ca$_3$(PO$_4$)$_2$ bands were observed; the sharp intensity and shoulder peaks for symmetric stretching were measured at ~947 and 969 cm^{-1} (ν_1 mode); bending P-O bands were measured at ~406, 441, and 481 cm^{-1} (ν_2 modes); stretching P-O bands at 1046 and 1089 cm^{-1} (ν_3 modes); and triply degenerate asymmetric P-O bending was measured at ~548, 612, and 627 cm^{-1} (ν_4 modes) [33,34]. In addition, peaks emerged for the *t*-ZrO$_2$ peaks at 145, 222, 263, 381, 473, and 637 cm^{-1}, and *m*-ZrO$_2$ peaks were observed at 178 and 189 cm^{-1}, corresponding to the Zr-O vibrations modes [35]. At 700 °C, the Raman spectra revealed the presence of an apatite phase, which was detected at 960 cm^{-1} to represent CDA (Ca/P ratio = 1.5). Moreover, major and minor boosted peaks are observed, which are attributed to the Zr-O vibration band of the dual phase of *t*-ZrO$_2$ and *m*-ZrO$_2$. The spectra observed at 900 °C demonstrated four different phases: β-Ca$_3$(PO$_4$)$_2$, *m*-ZrO$_2$, *t*-ZrO$_2$, and HA (Figure 3b). The inset reveals that the apatite phase is retained at the 962 cm^{-1} bands; the shoulder peaks of β-Ca$_3$(PO$_4$)$_2$ at 945 cm^{-1} revealed a minor shift to a higher wavenumber. Furthermore, a gradual increase in the *t*-ZrO$_2$ and *m*-ZrO$_2$ peaks corresponded to an increase in the ZrO$_2$ precursor concentration. The complete elimination of apatite bands occurred at 1100 °C (Figure 3c). The presence of β-Ca$_3$(PO$_4$)$_2$, *m*-ZrO$_2$, and *t*-ZrO$_2$ at 1100 °C was corroborated.
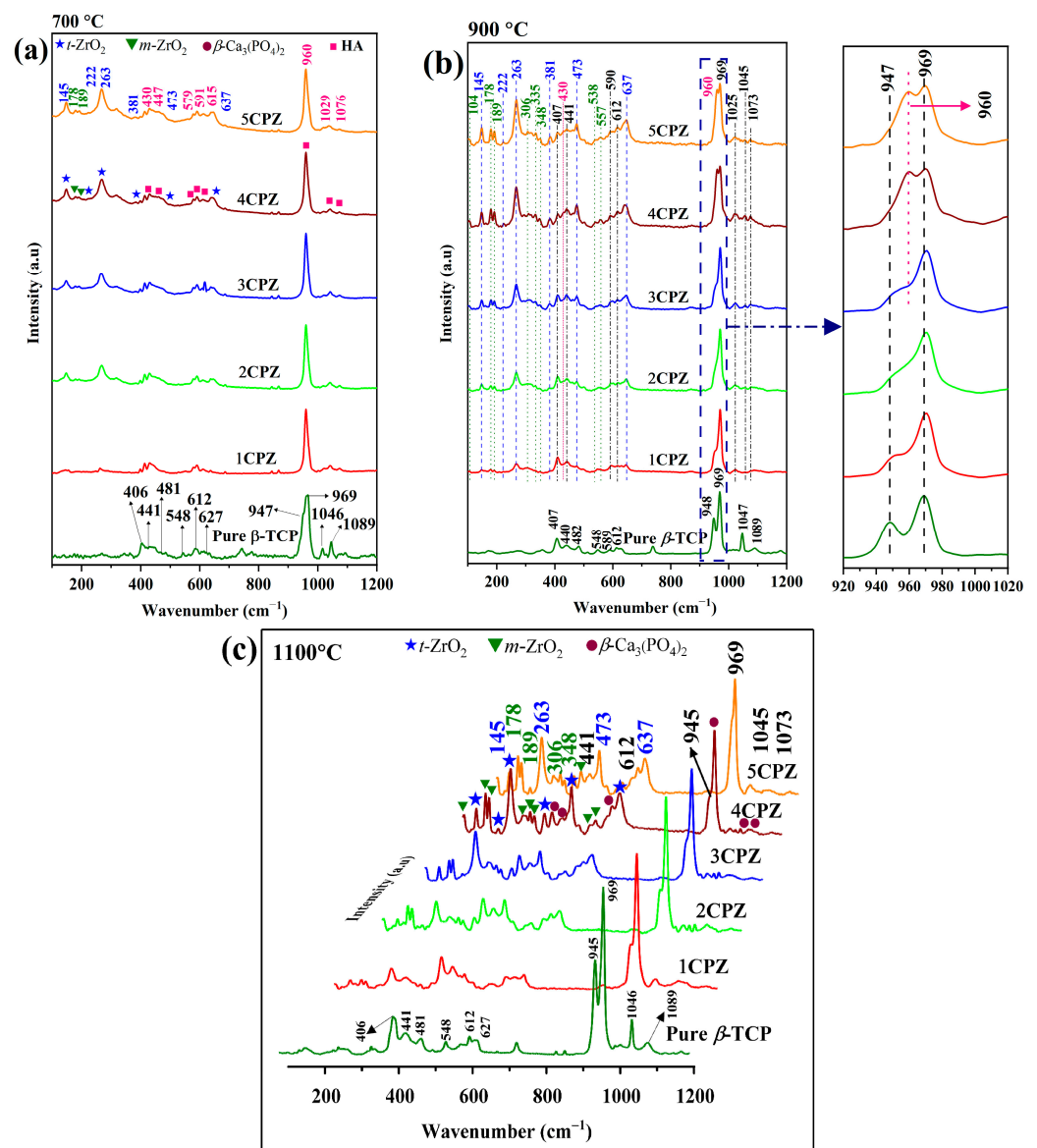
Figure 3. Raman spectra of the β-Ca$_3$(PO$_4$)$_2$–ZrO$_2$ composites after heat treatment at (**a**) 700 °C, (**b**) 900 °C, and (**c**) 1100 °C.

3.3. Fourier-Transform Infrared Spectroscopy

Infrared spectra were recorded for the β-Ca$_3$(PO$_4$)$_2$–ZrO$_2$ composites at 900 °C (Figure 4a) and 1100 °C (Figure 4b). The infrared spectra of β-Ca$_3$(PO$_4$)$_2$ for the P-O groups are prominent at ~943 and 973 cm^{-1} for symmetric P-O stretching (ν_1), ~430 cm^{-1} for doubly degenerate O−P−O bending (ν_2), ~1192 and 1206 cm^{-1} for triply degenerate asymmetric P-O stretching (ν_3), and ~555 and ~610 cm^{-1} for triply degenerate O-P-O bending (ν_4).
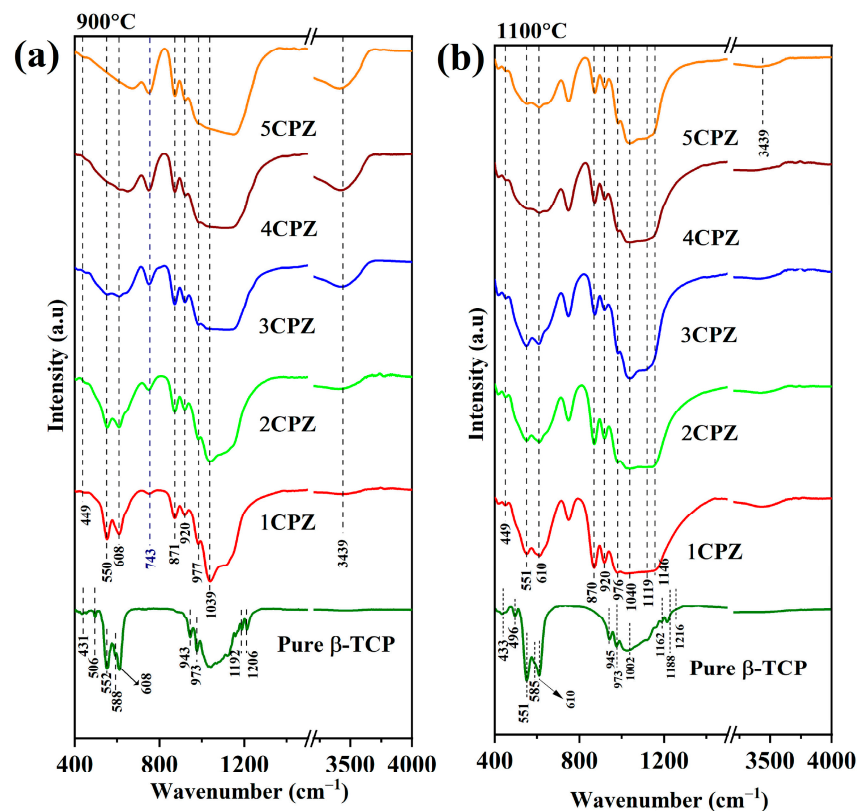
Figure 4. FT-IR spectra of the β-$Ca_3(PO_4)_2$–ZrO_2 composites after heat treatment at (**a**) 900 °C and (**b**) 1100 °C.

Infrared apatite spectra are observed at ~960 cm^{-1} for symmetric P−O stretching (ν_1); with regard to the OH group, they are observed from ~3200 to 3800 cm^{-1}, which corresponds to the HA peaks. The PO$_4$ tetrahedron groups correlate with the characteristic apatite peaks and the β-$Ca_3(PO_4)_2$ phase at 900 °C. Regarding the IR spectra, major peaks related to the hydroxyl group are observed at ~3439 cm^{-1} and 900 °C [36]. Moreover, sharp peaks for the Zr-O group in the monoclinic zirconia are observed at 743 cm^{-1}, corresponding to an increase in the concentration of zirconia precursor and a gradual increase in peak intensity [37]. Regarding the FTIR spectra recorded at 1100 °C, the apatite phase for the OH group is eliminated. However, a negligible change in the apatite phase is observed between 900 °C and 1100 °C, and a strong intensity peak is observed for the monoclinic zirconia at 1100 °C. Generally, the X-ray diffraction and Raman spectra corroborated the formation of the β-$Ca_3(PO_4)_2$–ZrO_2 composites.

3.4. Rietveld Refinement

The XRD, Raman, and FT-IR investigations confirm the phase formation of the β-$Ca_3(PO_4)_2$–ZrO_2 composites following consecutive heat treatments. Structural analysis was performed at 900 °C, 1000 °C, and 1100 °C for the β-$Ca_3(PO_4)_2$–ZrO_2 composites. The refinement diffraction pattern is presented in (Figure 5), whereas the refined phase composition, Rietveld agreement factors, and lattice parameters are listed in Tables 2 and 3. The refined 900 °C data confirm the presence of $Ca_{10}(PO_4)_6(OH)_2$, β-$Ca_3(PO_4)_2$, m-ZrO_2, and t-ZrO_2, corresponding to a crystalline $Ca_{10}(PO_4)_6(OH)_2$ hexagonal structure with a space group (P63/m (176)), β-$Ca_3(PO_4)_2$ with a rhombohedral structure (space group-R3c (137)), m-ZrO_2 with a monoclinic structure with a space group (P121/c1), and t-ZrO_2 with a hexagonal structure with a space group (P42/nmc) unit cell, respectively. The refined data agree with the phase formation of β-$Ca_3(PO_4)_2$–ZrO_2, which was confirmed at 1100 °C.
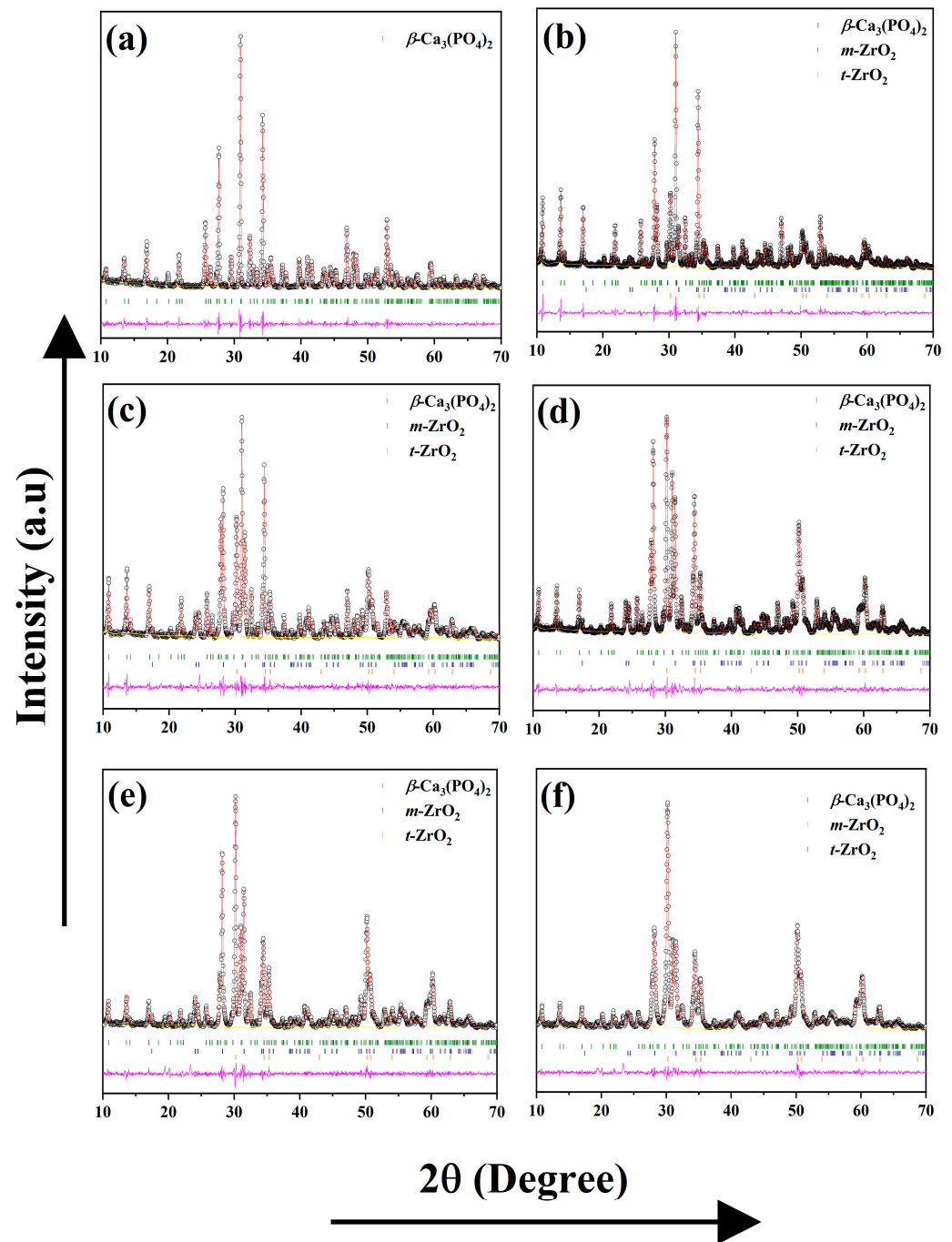
Figure 5. Rietveld refinement diffraction patterns for β-Ca$_3$(PO$_4$)$_2$–ZrO$_2$ composites at 1100 °C. (**a**) Pure TCP, (**b**) 1CPZ, (**c**) 2CPZ, (**d**) 3CPZ, (**e**) 4CPZ, and (**f**) 5CPZ. The calculated (red line), background (yellow line), and difference (magenta), as well as the Braggs of β-Ca$_3$(PO$_4$)$_2$ (olive lines), t-ZrO$_2$ (orange lines), and m-ZrO$_2$ (navy lines).

Table 2. Rietveld refinement agreement factors and phase composition data from the XRD pattern for three different temperatures.

Sample Code		Mineralogical Composition (Wt%)				Refinement Parameters			
		$Ca_{10}(PO_4)_6(OH)_2$	β-$Ca_3(PO_4)_2$	m-ZrO_2	t-ZrO_2	R_{wp}	R_p	χ^2	R_{Bragg}
900 °C	1CPZ	12.67 (2)	73.95 (5)	05.30 (1)	08.08 (2)	10.95	08.51	02.12	05.13
	2CPZ	14.58 (3)	57.86 (2)	11.28 (2)	16.28 (2)	10.58	07.89	01.51	04.64
	3CPZ	20.16 (4)	44.16 (2)	15.77 (2)	19.91 (4)	12.08	08.81	02.17	04.90
	4CPZ	25.87 (6)	29.96 (6)	20.22 (2)	23.95 (3)	12.78	09.18	02.53	05.41
	5CPZ	31.47 (8)	18.50 (1)	24.32 (8)	28.03 (9)	11.03	08.43	01.91	05.28
1000 °C	1CPZ	-	83.78 (1)	06.47 (1)	09.75 (6)	11.88	09.12	02.47	06.01
	2CPZ	-	69.31 (5)	12.25 (3)	18.44 (2)	10.91	08.45	02.38	06.16
	3CPZ	06.33 (2)	55.16 (2)	18.38 (1)	20.13 (2)	10.11	07.83	02.20	03.64
	4CPZ	11.27 (3)	39.46 (3)	22.40 (2)	26.87 (2)	10.80	08.18	02.68	05.16
	5CPZ	14.43 (6)	27.98 (2)	26.01 (1)	31.58 (2)	09.93	07.82	2.319	05.48
1100 °C	Pure TCP	-	100	-	-	07.15	08.44	1.114	04.29
	1CPZ	-	79.30 (3)	07.74 (2)	12.96 (2)	11.72	09.06	02.40	06.09
	2CPZ	-	66.03 (3)	13.68 (2)	20.29 (1)	10.54	08.26	2.236	05.20
	3CPZ	-	59.51 (2)	15.97 (5)	24.51 (2)	08.68	06.76	1.642	05.03
	4CPZ	-	42.49 (2)	19.92 (6)	25.03 (1)	09.84	07.53	02.18	05.71
	5CPZ	-	37.58 (6)	26.81 (4)	35.61 (5)	08.77	06.70	1.855	03.80

Table 3. Refined lattice parameters for the different phases for the pure TCP and five composites at 900 and 1100 °C.

Sample Code	Refined Lattice Parameter								
	$Ca_{10}(PO_4)_6(OH)_2$		β-$Ca_3(PO_4)_2$		m-ZrO_2			t-ZrO_2	
	$a = b$ axis	c-axis	$a = b$ axis	c-axis	a-axis	b-axis	c-axis	$a = b$ axis	c-axis
900 °C									
1CPZ	9.5532 (3)	6.8128 (3)	10.4112 (5)	37.4178 (2)	5.1186 (2)	5.1972 (4)	5.2963 (4)	3.5946 (5)	5.1914 (1)
2CPZ	9.5893 (2)	6.8037(3)	10.4086 (8)	37.3946 (3)	5.1460 (2)	5.2041 (2)	5.3156 (2)	3.5934 (4)	5.1891 (8)
3CPZ	9.5924 (8)	6.8199 (1)	10.4101 (1)	37.3925 (4)	5.1504 (2)	5.2047 (1)	5.3159 (2)	3.5924 (5)	5.1909 (1)
4CPZ	9.5636 (5)	6.7571 (6)	10.4015 (2)	37.3617 (7)	5.1496 (2)	5.1927 (1)	5.3159 (1)	3.5900 (5)	5.1851 (1)
5CPZ	9.5465 (5)	6.7788 (5)	10.4016 (2)	37.3638 (7)	5.1504 (1)	5.1988 (1)	5.3139 (2)	3.5940 (4)	5.1817 (9)
1100 °C									
Pure TCP	-	-	10.4384 (3)	37.4010 (1)	-	-	-	-	-
1CPZ	-	-	10.4203 (4)	37.3877 (1)	5.1481 (8)	5.2092 (9)	5.3124 (8)	3.5948 (3)	5.1868 (8)
2CPZ	-	-	10.4118 (4)	37.3669 (2)	5.1471 (4)	5.2090 (5)	5.3133 (5)	3.5936 (2)	5.1889 (6)
3CPZ	-	-	10.4078 (6)	37.3630 (2)	5.1476 (4)	5.2083 (4)	5.3135 (4)	3.5940 (2)	5.1864 (4)
4CPZ	-	-	10.4063 (7)	37.3600 (3)	5.1452 (4)	5.2075 (5)	5.3118(5)	3.5938(2)	5.1828 (4)
5CPZ	-	-	10.4023 (9)	37.3582 (4)	5.1465 (7)	5.2048 (9)	5.3137 (8)	3.5935 (3)	5.1827 (5)

The phase fractions at 900 °C from the refined data for the five different composites reveal a gradual increase in t-ZrO_2 and m-ZrO_2 content and a simultaneous reduction in β-$Ca_3(PO_4)_2$ and the apatite phase. The refined phase fractions at 1000 °C at 1CPZ and 2CPZ demonstrate a negligible apatite phase and a significant and steady increase in the β-$Ca_3(PO_4)_2$ phase fraction. The apatite phase is evident at 3CPZ, 4CPZ, and 5CPZ, which displays an increase in the phase fraction and a decrease in the β-$Ca_3(PO_4)_2$ phase. However, the t-ZrO_2 and m-ZrO_2 phases are dominant in the composites. In the comparative phase composition of β-$Ca_3(PO_4)_2$, t-ZrO_2, and m-ZrO_2, the complete elimination of the apatite

phase is observed at 1100 °C. The data of the refined lattice parameters reveal the refined phase fraction at 900 °C and 1100 °C. A considerable contraction in the lattice parameter of β-Ca$_3$(PO$_4$)$_2$, demonstrated in *a = b axis* and the *c-axis*, reveals marked differences in reductance compared with pure TCP; the decrease in the lattice parameters corresponds to an increase in ZrO$_2$ content at 900 °C and 1100 °C. The preferential occupancy factors that were refined at 1100 °C are listed in Table 4, which demonstrated that Zr^{4+} was accommodated at the Ca5 sites of the β-Ca$_3$(PO$_4$)$_2$ lattice throughout the composites. In contrast, the *t*-ZrO$_2$ and *m*-ZrO$_2$ lattice parameters exhibit no significant changes following an increase in the ZrO$_2$ phase contents.

Table 4. Refined occupancy factor of Zr^{4+} for Ca^{2+} accommodation in the composites. Young's modulus and hardness data were acquired from the β-Ca$_3$(PO$_4$)$_2$–ZrO$_2$ composites at 1100 °C.

Sample Code	Occupancy Factor	Nanoindentation Data	
	Ca^{2+} (5) Sites	Young's Modulus (GPa)	Hardness (GPa)
1CPZ	0.85 (2)	48.76 ± 02.51	01.79 ± 0.18
2CPZ	0.72 (9)	45.97 ± 01.38	01.59 ± 0.11
3CPZ	0.84 (2)	42.36 ± 02.08	01.51 ± 0.18
4CPZ	0.81 (5)	41.30 ± 04.09	01.36 ± 0.34
5CPZ	0.91 (3)	38.30 ± 02.75	01.30 ± 0.17

3.5. Morphological and Mechanical Features

The morphological characteristics of the β-Ca$_3$(PO$_4$)$_2$–ZrO$_2$ composite pellets heat treated at 1100 °C are indicated in (Figure 6). The grains in 1CPZ were randomly distributed throughout the microstructure and numerous voids were present. The grain growth in 5CPZ is haphazard and the grains are overlaid with pores; this indicates that their growth commenced at 1100 °C. The increase in grain distribution within the microstructure corresponds to an increase in the ZrO$_2$ concentration.

Moreover, energy-dispersive X-ray spectroscopy indicates that the elemental composition is dominated by Ca, Zr, P, and O. The element distribution in 1CPZ and 5CPZ is in good agreement with the refined phase fractions. The mechanical stability data from the nanoindentation test are listed in Table 4 and the load displacement profiles are shown in Figure 7. The loading and unloading profiles in all the compositions are irregular. Micropores and twining grains are evident in the microstructures of the composites, and it evinces the existence of the *t*-→ *m*-ZrO$_2$ toughening mechanism. The indentation profiles validate the stabilized zirconia grains' smooth loading and unloading profiles and an inadequate profile for the porous structure. However, the mechanical data reveal that Young's modulus and hardness decrease with an increase in the ZrO$_2$ precursor concentrations.
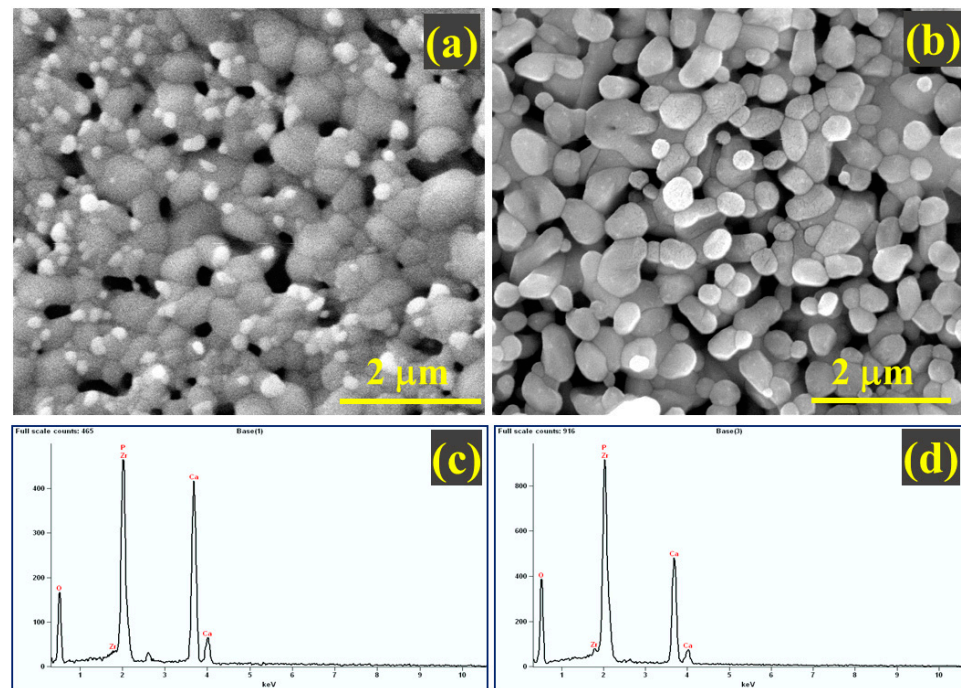
Figure 6. Microstructural features and energy-dispersive X-ray spectra of the β-Ca$_3$(PO$_4$)$_2$–ZrO$_2$ composites sintered at 1100 °C. (**a**,**b**) 1CPZ and 5CPZ micrographs, (**c**,**d**) corresponding EDS maps reveal the elemental composition: O, P, Ca, and Zr of 1CPZ and 5CPZ, respectively.
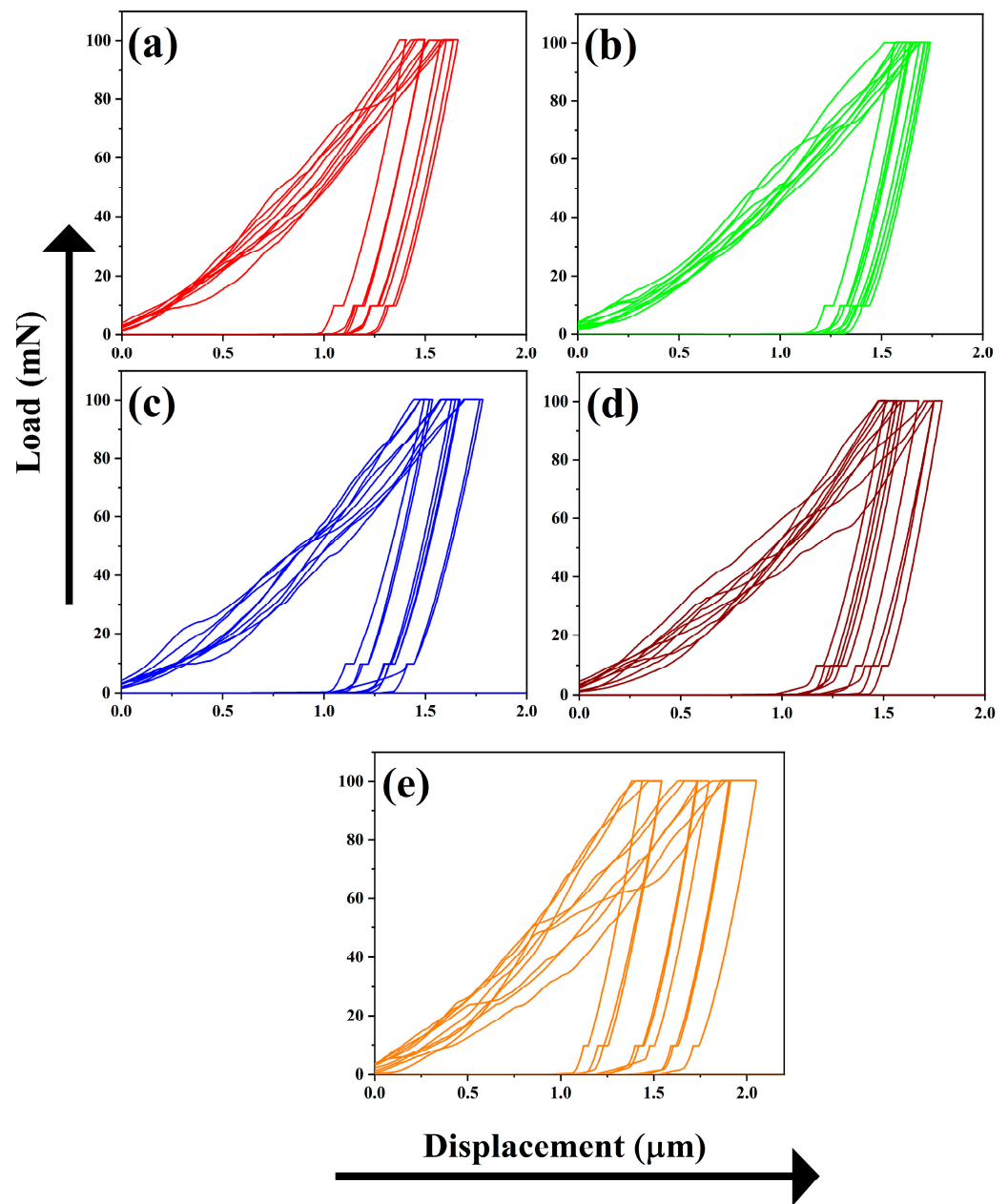
Figure 7. Nanoindentation test representing the five different β-Ca$_3$(PO$_4$)$_2$–ZrO$_2$ composites sintered at 1100 °C. (**a**) 1CPZ, (**b**) 2CPZ, (**c**) 3CPZ, (**d**) 4CPZ, and (**e**) 5CPZ.

4. Discussion

The results revealed the formation of a stable phase following the formation of the β-Ca$_3$(PO$_4$)$_2$–ZrO$_2$ composite mixtures with varying Zr concentrations through the wet precipitation method. The crystallization of ZrO$_2$ for the t-ZrO$_2$ and CDA phases commenced at 700 °C. The conversion of the CDA (Ca/P ratio = 1.5) to the β-Ca$_3$(PO$_4$)$_2$ phase occurred at ~780 °C, as reported earlier [38,39]. Numerous cation materials have recently been investigated for the β-Ca$_3$(PO$_4$)$_2$ composites and varied outcomes have been reported [40,41]. The phase changes for the individual cation, which delays the conversion of CDA to β-Ca$_3$(PO$_4$)$_2$. Due to the unique cation physiognomies, phase conversion occurs in Al$_2$O$_3$, TiO$_2$, and Fe$_2$O$_3$; ZnO, CeO$_2$, and Y$_2$O$_3$ delay the apatite transformation [42]. In contrast, β-Ca$_3$(PO$_4$)$_2$ with zirconia-composite additives demonstrates the influence of the Dy^{3+}, Y^{3+}, and Gd^{3+} stabilizers, which delay the apatite phase transformation following an increase in temperature [43,44]. Furthermore, t-ZrO$_2$ and m-ZrO$_2$ are observed throughout the

composites. The t-ZrO_2 phase stabilization is validated by (1) the moiety of a hydroxyl group and absorbed water molecule, which prompts the t-ZrO_2 phase at low-temperature sintering, and (2) the fact that Ca^{2+} ions may be partially cleaved in the β-$Ca_3(PO_4)_2$ lattice site. The partially cleaved Ca^{2+} ions were accommodated in the Zr^{4+} lattice sites, which emerged to form the t-ZrO_2 phase. The scarcity of Ca^{2+} ions is attributed to the m-ZrO_2 phase transformation [45,46].

The phase changes for the individual cation, which delays the conversion of CDA to β-$Ca_3(PO_4)_2$. Due to the unique cation physiognomies, phase conversion occurs in Al_2O_3, TiO_2, and Fe_2O_3; ZnO, CeO_2, and Y_2O_3 delay the apatite transformation. In contrast, β-$Ca_3(PO_4)_2$ with zirconia-composite additives demonstrates the influence of the Dy^{3+}, Y^{3+}, and Gd^{3+} stabilizers, which delay the apatite phase transformation following an increase in temperature. Furthermore, t-ZrO_2 and m-ZrO_2 are observed throughout the composites. The t-ZrO_2 phase stabilization is validated by (1) the moiety of a hydroxyl group and absorbed water molecule, which prompts the t-ZrO_2 phase at low-temperature sintering, and (2) the fact that Ca^{2+} ions may be partially cleaved in the β-$Ca_3(PO_4)_2$ lattice site. The partially cleaved Ca^{2+} ions were accommodated in the Zr^{4+} lattice sites, which emerged to form the t-ZrO_2 phase. The scarcity of Ca^{2+} ions is attributed to the m-ZrO_2 phase transformation.

The phase fraction characterizes the β-$Ca_3(PO_4)_2$–ZrO_2 composites at the three different temperatures, demonstrating the decomposition of CDA following sequential heat treatments. Consequently, a steady increase in the t-ZrO_2 and m-ZrO_2 phases and a decrease in β-$Ca_3(PO_4)_2$ were observed. The Raman spectra in Figure 3 indicate a potential deterioration in the apatite phase following thermal treatment of the composites. The gradual increase in t-ZrO_2 and m-ZrO_2 in the composite mixtures is evident. Extensive cation inclusion and substitution, from monovalent to tetravalent cations, in the β-$Ca_3(PO_4)_2$ lattice reportedly result in thermal stability and retained biological functions [47,48]. Depending on the valence effect and ionic size, small and large cations replace the Ca^{2+}(sites). The occupancy factor of Zr^{4+} (0.79 Å) at the Ca^{2+} (1.00 Å) site accommodated the Ca^{2+} (5) locations in the β-$Ca_3(PO_4)_2$ lattice. However, a minimum amount of Zr^{4+} can occupy the Ca^{2+} (5) sites and the excess Zr^{4+} ions form the ZrO_2 composites. However, the lattice parameters exhibit consistent contractions in the β-$Ca_3(PO_4)_2$ lattice sites, which affect the incorporation of the Zr^{4+} ions. The Ca^{2+} ions are deficient in the β-$Ca_3(PO_4)_2$ structure; their action on the Zr^{4+} ions leads to crystallization and the formation of t-ZrO_2. The twofold mixture of the t-ZrO_2 and m-ZrO_2 phases is achieved by the addition of CaO (from 0.5 to 1.2 mol%), and the stable t-ZrO_2 phase is obtained by the addition of more than 9.3 mol% CaO [49]. Moreover, the results show the lack of a secondary phase formation. This confirms a CaO deficiency, which prevents the formation of $CaZrO_3$ as an end product.

The morphology of β-$Ca_3(PO_4)_2$–ZrO_2 is irregularly arranged grains, with numerous voids present in 1CPZ and 5CPZ, which results in poor mechanical stability. The uneven grains and pores in the microstructure are due to the thermal expansion of individual grains in the composite mixtures. The hardness and Young's modulus from the nanoindentation data exhibit a decrease following the gradual increase in precursor concentration. The drastic decrease in elastic modulus and hardness with the increasing porosity of the composites suggests that binding energy has been released. This indicates that increasing the density and toughness is required to constrain grain growth, thus limiting the t-$ZrO_2 \rightarrow m$-ZrO_2 phase change following thermal treatment. However, the hardness and Young's modulus of the β-$Ca_3(PO_4)_2$–ZrO_2 suggest better mechanical stability than natural bone [50].

5. Conclusions

A simple co-precipitation approach presents the formation of the β-$Ca_3(PO_4)_2$–ZrO_2 composites with varying compositional ratios. The phase transition from CDA to pure β-$Ca_3(PO_4)_2$ occurs at 1100 °C. The compositional ratios comprise a wide range of Ca^{2+} and Zr^{4+} precursor concentrations. Zr^{4+} is preferentially accommodated at the β-$Ca_3(PO_4)_2$ crystal structure and its continuous accumulation leads to the formation of ZrO_2. Adding

zirconia beyond the saturation limit of β-$Ca_3(PO_4)_2$ led to the crystallization of m-ZrO_2 and t-ZrO_2, and further additions resulted in a sharp increase in the ZrO content. The surface morphological features include irregular grains with numerous voids, and Ca^{2+}, P^{+5}, Zr^{4+}, and O^{2-} are uniformly distributed throughout the composites. Tests on the mechanical stability confirm the deterioration in Young's modulus and hardness following augmentation of the ZrO_2 content.

Author Contributions: Conceptualization, N.K.P.; methodology, N.K.P., H.L., J.M.Y., and S.Y.N.; investigation, N.K.P.; data curation, N.K.P., H.L., J.M.Y.; writing—original draft preparation, N.K.P.; writing—review and editing, S.Y.N.; visualization, N.K.P., H.L., J.M.Y.; supervision, S.Y.N.; project administration, J.M.Y., S.Y.N.; funding acquisition, H.L., S.Y.N. All authors have read and agreed to the published version of the manuscript.

Institutional Review Board Statement: Not applicable.

Informed Consent Statement: Not applicable.

Data Availability Statement: The data that support the findings of this study are available upon reasonable request from the authors.

Conflicts of Interest: The authors declare no conflict of interest.

Nomenclature List

β-TCP (β-$Ca_3(PO_4)_2$)	Beta-tricalcium phosphate
TCP	Tricalcium phosphate
ZrO_2	Zirconia
t-ZrO_2	Tetragonal zirconia
m-ZrO_2	Monoclinic zirconia
HA	Hydroxyapatite
CaO	Calcium oxide
$CaZrO_3$	Calcium zirconate
$Ca_4(PO_4)_2O$	Tetracalcium phosphate
α-$Ca_3(PO_4)_2$	Alpha-tricalcium phosphate
Ca^{2+}	Calcium
P^{+5}	Phosphorus
Zr^{4+}	Zirconium
O^{2-}	Oxygen
Y^{3+}	Yttrium
Gd^{3+}	Gadolinium
Dy^{3+}	Dysprosium
TiO_2	Titanium dioxide
Al_2O_3	Aluminum oxide
CDA	Calcium deficient apatite
CIF	Crystallographic Information File
XRD	X-ray diffraction
FTIR	Fourier transform infrared
GPa	Gigapascal

References

1. Wagner, W.R.; Sakiyama-Elbert., S.E.; Zhang, G.; Yaszemski, M.J. *Biomaterials Science: An Introduction to Materials in Medicine*; Academic Press: Cambridge, MA, USA, 2020.
2. Alvarez Echazu, M.I.; Perna, O.; Olivetti, C.E.; Antezana, P.E.; Municoy, S.; Tuttolomondo, M.V.; Galdoporpora, J.M.; Alvarez, G.S.; Olmedo, D.G.; Desimone, M.F. Recent Advances in Synthetic and Natural Biomaterials-Based Therapy for Bone Defects. *Macromol. Biosci.* **2022**, E2100383. [CrossRef] [PubMed]
3. Roohani, I.; Yeo, G.C.; Mithieux, S.M.; Weiss, A.S. Emerging concepts in bone repair and the premise of soft materials. *Curr. Opin. Biotechnol.* **2021**, *74*, 220–229. [CrossRef] [PubMed]

4. Trojani, M.C.; Santucci-Darmanin, S.; Breuil, V.; Carle, G.F.; Pierrefite-Carle, V. Autophagy and bone diseases. *Jt. Bone Spine* **2021**, *89*, 105301. [CrossRef] [PubMed]

5. Silvio, L.D. *Cellular Response to Biomaterials*; Woodhead Publishing: Sawston, UK, 2009.

6. Black, J. *Biological Performance of Materials: Fundamentals of Biocompatibility*; CRC Press: Boca Raton, FL, USA, 2005.

7. Chawla, K. *Biomaterials for Tissue Engineering*; Springer: Berlin/Heidelberg, Germany, 2018.

8. Tanzi, M.; Farè, S.; Candiani, G. *Foundations of Biomaterials Engineering*; Academic Press: Cambridge, MA, USA, 2019.

9. Elliott, J.C. *Structure and Chemistry of the Apatites and Other Calcium Orthophosphates*; Elsevier: Amsterdam, The Netherlands, 2013.

10. Lee, H.; Yoo, J.M.; Ponnusamy, N.K.; Nam, S.Y. 3D-printed hydroxyapatite/gelatin bone scaffolds reinforced with graphene oxide: Optimized fabrication and mechanical characterization. *Ceram. Int.* **2022**, *48*, 10155–10163. [CrossRef]

11. Ratner, B.D.; Hoffman, A.S.; Schoen, F.J.; Lemons, J.E. *Biomaterials Science: An Introduction to Materials in Medicine*; Academic Press: San Diego, CA, USA, 2004.

12. Ducheyne, P. *Comprehensive Biomaterials*; Elsevier: Amsterdam, The Netherlands, 2015; Volume 1.

13. Cao, Y.; Shi, T.; Jiao, C.; Liang, H.; Chen, R.; Tian, Z.; Zou, A.; Yang, Y.; Wei, Z.; Wang, C.; et al. Fabrication and properties of zirconia/hydroxyapatite composite scaffold based on digital light processing. *Ceram. Int.* **2020**, *46*, 2300–2308. [CrossRef]

14. Wong, J.Y.; Bronzino, J.D.; Wong, J.Y.; Bronzino, J.D. *Biomaterials*; CRC Press: Boca Raton, FL, USA, 2007.

15. Chevalier, J. What future for zirconia as a biomaterial? *Biomaterials* **2006**, *27*, 535–543. [CrossRef]

16. Callister, W.D.; Rethwisch, D.G. *Materials Science and Engineering an Introduction*, 10th ed.; John Wiley & Sons, Inc.: Hoboken, NJ, USA, 2018.

17. Alao, A.-R.; Yin, L. Loading rate effect on the mechanical behavior of zirconia in nanoindentation. *Mater. Sci. Eng. A* **2014**, *619*, 247–255. [CrossRef]

18. Cao, Y.; Li, C.; Xia, Y.; Ren, K.; Zhu, S. Study on the fabrication and mechanical properties of HAp-3YSZ composites by flash sintering. *Ceram. Int.* **2022**. [CrossRef]

19. Shadianlou, F.; Foorginejad, A.; Yaghoubinezhad, Y. Fabrication of zirconia/reduced graphene oxide/hydroxyapatite scaffold by rapid prototyping method and its mechanical and biocompatibility properties. *Ceram. Int.* **2022**, *48*, 7031–7044. [CrossRef]

20. Brzezińska-Miecznik, J.; Haberko, K.; Sitarz, M.; Bućko, M.M.; Macherzyńska, B.; Lach, R. Natural and synthetic hydroxyapatite/zirconia composites: A comparative study. *Ceram. Int.* **2016**, *42*, 11126–11135. [CrossRef]

21. Kumar, V.A.; Rama Murty Raju, P.; Ramanaiah, N.; Siriyala, R. Effect of ZrO_2 content on the mechanical properties and microstructure of HAp/ZrO_2 nanocomposites. *Ceram. Int.* **2018**, *44*, 10345–10351. [CrossRef]

22. Catauro, M.; Bollino, F.; Tranquillo, E.; Tuffi, R.; Dell'Era, A.; Ciprioti, S.V. Morphological and thermal characterization of zirconia/hydroxyapatite composites prepared via sol-gel for biomedical applications. *Ceram. Int.* **2019**, *45*, 2835–2845. [CrossRef]

23. Caroff, F.; Oh, K.S.; Famery, R.; Boch, P. Sintering of TCP-TiO2 biocomposites: Influence of secondary phases. *Biomaterials* **1998**, *19*, 1451–1454. [CrossRef]

24. Castkova, K.; Hadraba, H.; Matousek, A.; Roupcova, P.; Chlup, Z.; Novotna, L.; Cihlar, J. Synthesis of Ca,Y-zirconia/hydroxyapatite nanoparticles and composites. *J. Eur. Ceram. Soc.* **2016**, *36*, 2903–2912. [CrossRef]

25. Nandha Kumar, P.; Kannan, S. Sequential elucidation of the beta-$Ca_3(PO_4)_2$/TiO_2 composite development from the solution precursors. *Dalton Trans.* **2017**, *46*, 3229–3239. [CrossRef] [PubMed]

26. Nandha Kumar, P.; Ferreira, J.M.F.; Kannan, S. Phase transition mechanisms involved in the formation of structurally stable β-$Ca_3(PO_4)_2$-α-Al_2O_3 composites. *J. Eur. Ceram. Soc.* **2017**, *37*, 2953–2963. [CrossRef]

27. Nandha Kumar, P.; Ferreira, J.M.; Kannan, S. Formation Mechanisms in beta-$Ca_3(PO_4)_2$-ZnO Composites: Structural Repercussions of Composition and Heat Treatments. *Inorg. Chem.* **2017**, *56*, 1289–1299. [CrossRef]

28. Downs, R.T.; Hall-Wallace, M. The American Mineralogist crystal structure database. *American Mineralogist* **2003**, *88*, 247–250.

29. Yashima, M.; Sakai, A.; Kamiyama, T.; Hoshikawa, A. Crystal structure analysis of β-tricalcium phosphate $Ca_3(PO_4)_2$ by neutron powder diffraction. *J. Solid State Chem.* **2003**, *175*, 272–277. [CrossRef]

30. Wilson, R.M.; Elliott, J.C.; Dowker, S.E.P. Rietveld refinement of the crystallographic structure of human dental enamel apatites. *Am. Mineral.* **1999**, *84*, 1406–1414. [CrossRef]

31. Howard, C.J.; Hill, R.J.; Reichert, B.E. Structures of ZrO_2 polymorphs at room temperature by high-resolution neutron powder diffraction. *Acta Crystallogr. Sect. B Struct. Sci.* **1988**, *44*, 116–120. [CrossRef]

32. Smith, D.K.; Newkirk, W. The crystal structure of baddeleyite (monoclinic ZrO_2) and its relation to the polymorphism of ZrO_2. *Acta Crystallogr.* **1965**, *18*, 983–991. [CrossRef]

33. de Aza, P.N.; Santos, C.; Pazo, A.; de Aza, S.; Cuscó, R.; Artús, L. Vibrational Properties of Calcium Phosphate Compounds. 1. Raman Spectrum of β-Tricalcium Phosphate. *Chem. Mater.* **1997**, *9*, 912–915. [CrossRef]

34. de Aza, P.N.; Guitián, F.; Santos, C.; de Aza, S.; Cuscó, R.; Artús, L. Vibrational Properties of Calcium Phosphate Compounds. 2. Comparison between Hydroxyapatite and β-Tricalcium Phosphate. *Chem. Mater.* **1997**, *9*, 916–922. [CrossRef]

35. Ishigame, M.; Sakurai, T. Temperature Dependence of the Raman Spectra of ZrO_2. *J. Am. Ceram. Soc.* **1977**, *60*, 367–369. [CrossRef]

36. Raynaud, S.; Champion, E.; Bernache-Assollant, D.; Thomas, P. Calcium phosphate apatites with variable Ca/P atomic ratio I. Synthesis, characterisation and thermal stability of powders. *Biomaterials* **2002**, *23*, 1065–1072. [CrossRef]

37. Aktug, S.L.; Kutbay, I.; Usta, M. Characterization and formation of bioactive hydroxyapatite coating on commercially pure zirconium by micro arc oxidation. *J. Alloys Compd.* **2017**, *695*, 998–1004. [CrossRef]

38. Gibson, I.R.; Rehman, I.; Best, S.M.; Bonfield, W. Characterization of the transformation from calcium-deficient apatite to beta-tricalcium phosphate. *J. Mater. Sci. Mater. Med.* **2000**, *11*, 533–539. [CrossRef]

39. Mortier, A.; Lemaitre, J.; Rodrique, L.; Rouxhet, P.G. Synthesis and thermal behavior of well-crystallized calcium-deficient phosphate apatite. *J. Solid State Chem.* **1989**, *78*, 215–219. [CrossRef]

40. Yoshida, K.; Hyuga, H.; Kondo, N.; Kita, H.; Sasaki, M.; Mitamura, M.; Hashimoto, K.; Toda, Y. Substitution Model of Monovalent (Li, Na, and K), Divalent (Mg), and Trivalent (Al) Metal Ions for beta-Tricalcium Phosphate. *J. Am. Ceram. Soc.* **2006**, *89*, 688–690. [CrossRef]

41. Meenambal, R.; Nandha Kumar, P.; Poojar, P.; Geethanath, S.; Kannan, S. Simultaneous substitutions of Gd^{3+} and Dy^{3+} in β-$Ca_3(PO_4)_2$ as a potential multifunctional bio-probe. *Mater. Des.* **2017**, *120*, 336–344. [CrossRef]

42. Nandha Kumar, P.; Mishra, S.K.; Kannan, S. Structural Perceptions and Mechanical Evaluation of beta-$Ca_3(PO_4)_2$/c-CeO_2 Composites with Preferential Occupancy of Ce^{3+} and Ce^{4+}. *Inorg. Chem.* **2017**, *56*, 3600–3611. [CrossRef] [PubMed]

43. Kumar, P.N.; Kannan, S.; Ferreira, J.M.F. Combined Occupancy of Gadolinium at the Lattice Sites of β-$Ca_3(PO_4)_2$ and t-ZrO_2 Crystal Structures. *Eur. J. Inorg. Chem.* **2020**, *2020*, 1163–1171. [CrossRef]

44. Nandha Kumar, P.; Subramanian, S.; Vijayalakshmi, U.; Kannan, S. Simultaneous accommodation of Dy^{3+} at the lattice site of β-$Ca_3(PO_4)_2$ and t-ZrO_2 mixtures: Structural stability, mechanical, optical, and magnetic features. *J. Am. Ceram. Soc.* **2020**, *103*, 3528–3540. [CrossRef]

45. Heimann, R.B.; Vu, T.A. Effect of CaO on thermal decomposition during sintering of composite hydroxyapatite–zirconia mixtures for monolithic bioceramic implants. *J. Mater. Sci. Lett.* **1997**, *16*, 437–439. [CrossRef]

46. Kannan, S.; Rocha, J.H.G.; Ventura, J.M.G.; Lemos, A.F.; Ferreira, J.M.F. Effect of Ca/P ratio of precursors on the formation of different calcium apatitic ceramics—An X-ray diffraction study. *Scr. Mater.* **2005**, *53*, 1259–1262. [CrossRef]

47. Bohner, M.; Santoni, B.L.G.; Dobelin, N. beta-tricalcium phosphate for bone substitution: Synthesis and properties. *Acta Biomater.* **2020**, *113*, 23–41. [CrossRef]

48. Gomes, S.; Nedelec, J.-M.; Jallot, E.; Sheptyakov, D.; Renaudin, G. Unexpected Mechanism of Zn2+ Insertion in Calcium Phosphate Bioceramics. *Chem. Mater.* **2011**, *23*, 3072–3085. [CrossRef]

49. Emam, W.I.; Mabied, A.F.; Hashem, H.M.; Selim, M.M.; El-Shabiny, A.M.; Ahmed Farag, I.S. Controlling polymorphic structures and investigating electric properties of Ca-doped zirconia using solid state ceramic method. *J. Solid State Chem.* **2015**, *228*, 153–159. [CrossRef]

50. Hengsberger, S.; Kulik, A.; Zysset, P. Nanoindentation discriminates the elastic properties of individual human bone lamellae under dry and physiological conditions. *Bone* **2002**, *30*, 178–184. [CrossRef]